Journal of Molecular Catalysis A: Chemical 329 (2010) 64–70

Contents lists available at ScienceDirect

Journal of Molecular Catalysis A: Chemical

journal homepage: www.elsevier.com/locate/molcata

The dehydrogenation of ethylbenzene with CO_2 over $V_2O_5/Ce_xZr_{1-x}O_2$ prepared with different methods

Chan Wang[a], Wei-Bin Fan[b], Zhao-Tie Liu[a], Jian Lu[a], Zhong-Wen Liu[a,*], Zhang-Feng Qin[b], Jian-Guo Wang[b]

[a] Key Laboratory of Applied Surface and Colloid Chemistry, School of Chemistry & Materials Science, Shaanxi Normal University, No. 199, South Chang'an Rd., Xi'an 710062, China
[b] State Key Laboratory of Coal Conversion, Institute of Coal Chemistry, Chinese Academy of Sciences, Taiyuan 030001, China

ARTICLE INFO

Article history:
Received 19 March 2010
Received in revised form 12 June 2010
Accepted 17 June 2010
Available online 25 June 2010

Keywords:
Ethylbenzene dehydrogenation
CO_2
$Ce_xZr_{1-x}O_2$ solid solution
Vanadia

ABSTRACT

The high-surface-area $Ce_xZr_{1-x}O_2$ composite oxides with various compositions were prepared with modified hydrothermal and sol–gel methods, respectively. Different amounts of vanadia were loaded via an incipient wetness technique for the preparation of the $V_2O_5/Ce_xZr_{1-x}O_2$. The prepared samples were subjected to the dehydrogenation of ethylbenzene (EB) in the presence of CO_2 in a fixed-bed reactor under the conditions of T = 823 K, P = 1 atm, and CO_2/BE molar ratio = 20. The hydrothermal $Ce_xZr_{1-x}O_2$ loaded with 6 wt.% V_2O_5 showed obviously higher EB conversion than the 6 wt.% $V_2O_5/Ce_xZr_{1-x}O_2$(sol–gel) although similar styrene selectivity was obtained. Moreover, the V_2O_5 loadings and the Ce/Zr ratios had clear influence on both the activity and the stability of the catalyst. Irrespective of the preparation methods and Ce/Zr ratios, XRD results indicate that nanocrystalline $Ce_xZr_{1-x}O_2$ solid solution was exclusively formed. Independent of the Ce/Zr ratios, the $Ce_xZr_{1-x}O_2$ prepared with hydrothermal method was composed of pure cubic phase while mixed phases were observed for the sol–gel samples as revealed from Raman results. With increasing vanadia loadings from 3 to 15 wt.%, different forms of vanadium species, such as vanadates and crystalline V_2O_5, were observed from Raman spectra. Irrespective of the V_2O_5 loadings, a single-step reduction of the supported V_2O_5 was revealed from the TPR patterns. Based on these and the TGA/DSC analysis of the used catalysts, the experimental results were extensively discussed and tentatively explained.

1. Introduction

In recent years, the utilization of CO_2 as a soft oxidant has received considerable attentions with the development of green chemistry and the much concern on the greenhouse effect of CO_2. Among the reactions investigated, the ethylbenzene (EB) dehydrogenation to styrene (ST) in the presence of CO_2 has attracted much attention and is still being continuously focused on [1–5] because of the following reasons: (1) the catalytic dehydrogenation of EB is one of the most important top 10 industrial processes; (2) the dehydrogenation of EB in the presence of CO_2 is energetically and thermodynamically more favorable than the present commercial process using overheated steam. However, the commercial Fe–K catalyst is not effective for the EB dehydrogenation in the presence of CO_2. Thus, much work has been done on the development of suitable catalyst [6–9], and vanadium oxide is found to exhibit good performance [10–13]. Although the mechanism for the EB dehydrogenation in the presence of CO_2 is still under debate, the higher performance of the vanadium oxide can be explained based on the redox mechanism (Mars–van Krevelen mechanism)[14,15].

Depending on the preparation methods and crystal structure, the high oxygen storage capacity (OSC) of ceria doped with zirconia is the main factor for its high performance in three-way catalyst [16]. Indeed, zirconia or ceria-zirconia is found to be active for catalyzing the oxidative dehydrogenation of EB with CO_2 [6]. Moreover, a correlation between the concentration of surface Ce^{4+}–O–Ce^{3+} defects and the rate for the oxidative dehydrogenation of EB with N_2O is revealed recently [17].

These understandings, i.e., the redox mechanism of the titled reaction and the excellent redox properties of vanadia and ceria-zirconia, motivated us to investigate the catalytic properties of the $V_2O_5/Ce_xZr_{(1-x)}O_2$ catalyst for the oxidative dehydrogenation of EB with CO_2. As the compositions and preparation methods of $Ce_xZr_{(1-x)}O_2$ are important factors for determining its crystal structure, a series of $Ce_xZr_{(1-x)}O_2$ with various Ce/Zr ratios were prepared with sol–gel and hydrothermal methods. A clear and complex effect of $Ce_xZr_{(1-x)}O_2$ on the activity and stability of V_2O_5 in oxidative dehydrogenation of EB with CO_2 is observed.

* Corresponding author. Tel.: +86 29 8530 3200; fax: +86 29 8530 7774.
E-mail address: zwliu@snnu.edu.cn (Z.-W. Liu).

1381-1169/$ – see front matter © 2010 Elsevier B.V. All rights reserved.
doi:10.1016/j.molcata.2010.06.019

2. Experimental

2.1. Catalyst preparation

The $Ce_xZr_{(1-x)}O_2$ samples were prepared with two methods, i.e., modified sol–gel and hydrothermal methods. The sol–gel procedure used in this work was as follows. To 100 mL absolute ethanol, the total amount of 0.02 mol cerium nitrate and zirconium nitrate with a desired Ce/Zr molar ratio was added. Separately, 0.006 mol of cetyltrimethyl ammonium bromide (CTAB) was dissolved in 50 mL absolute ethanol. At a room temperature, the two solutions were mixed and digested under stirring for 48 h. After this, the solvent was evaporated at 353 K. Finally, the $Ce_xZr_{(1-x)}O_2$ was obtained by drying and calcining the solid at 353 K for 12 h and 823 K for 4 h, respectively. In one case, to evaluate the effect of catalyst calcination temperature on the catalytic activity for the titled reaction, the 6 wt.% V_2O_5 supported on $Ce_{0.4}Zr_{0.6}O_2$ prepared with sol–gel method was calcined at 773, 823, 873, and 923 K for 4 h, respectively.

In the case of the hydrothermal method, polyethylene glycol (PEG, molecular weight of 6000) was firstly dissolved in a certain amount of deionized water followed by the addition of zirconium oxynitrate and cerium nitrate with the (Ce + Zr)/PEG molar ratio of 25. Then, additional deionized water was added to adjust the total concentration of the cerium and zirconium to be 0.2 mol L^{-1}. When a clear solution was formed, aqueous ammonia (5 mol L^{-1}) as a precipitation agent was added under stirring until a pH of 10.5. After further stirring for 2 h, it was transferred into a PTFE-lined stainless steel autoclave and aged under static conditions at 383 K for 72 h. Finally, the precipitate was recovered by centrifugation and washed extensively with deionized water. After drying at 373 K for 10 h, the sample was calcined at 823 K for 4 h to yield the final product.

The $V_2O_5/Ce_xZr_{(1-x)}O_2$ catalysts were prepared by an incipient wetness method via dipping the $Ce_xZr_{(1-x)}O_2$ fine powders into the aqueous solution of NH_4VO_3 along with oxalic acid. After drying at 373 K for 5 h, the catalyst was calcined at 823 K for 4 h if it is not specified.

2.2. Characterization

The surface areas of the materials were determined by the BET method on the automatic Micromeritics ASAP 2020 M. Before measurement, the samples were degassed at 573 K for 4 h, and the N_2 adsorption/desorption was performed at 77 K.

X-ray diffraction (XRD) patterns were recorded on a Rigaku X-ray diffractometer (D/Max 2550VB+/PC) equipped with Cu $K\alpha$ radiation (λ = 1.5406 Å) and Ni filter. The applied voltage and current were 30 kV and 40 mA, respectively. The samples were scanned from 2θ of 20–80° with a step size of 0.02° and a counting time of 2.5 s per step.

The laser Raman spectra were collected under ambient conditions on the dispersive Raman spectrometer (model ALMEGA-TM, Therm Nicolet) in the range of 100–1200 cm^{-1} (2 cm^{-1} resolution) with the excitation source laser beam of 532 nm.The reduction behavior of the composite oxides was investigated by hydrogen temperature-programmed reduction (TPR) in a Micromeritics Autochem 2920 instrument. Firstly, 50 mg of each sample was loaded and flushed with an Ar flow of 30 mL min^{-1} at room temperature for 2 h. TPR was performed from room temperature to 1003 K at a temperature ramp of 10 K min^{-1} under 30 mL min^{-1} flow of 10 vol.% H_2 in Ar. After condensing the water formed in an iso-propanol/liquid N_2 trap, the effluent was monitored with a TCD detector.To determine the properties of the coke deposited over the used catalysts, thermogravimetric analyses and differential scanning calorimetry (TGA/DSC) were performed on a Q600SDT Thermoanalyzer System (TA Instruments). About 10 mg sample placed in a DSC pan was heated from 323 to 823 K at a scanning rate of 10 K min^{-1} under a constant flow of dry air (100 mL min^{-1}).

Table 1
BET surface areas of the solid solutions.

	BET surface area (m^2/g)	
	Sol–gel method	Hydrothermal method
$Ce_{0.3}Zr_{0.7}O_2$	68	128
$Ce_{0.4}Zr_{0.6}O_2$	89	120
$Ce_{0.5}Zr_{0.5}O_2$	93	131
$Ce_{0.6}Zr_{0.4}O_2$	80	114
$Ce_{0.7}Zr_{0.3}O_2$	75	115

Table 2
BET surface areas of the catalysts[a].

Samples	BET surface area (m^2/g)
3 wt.% $V_2O_5/Ce_{0.3}Zr_{0.7}O_2$	100
6 wt.% $V_2O_5/Ce_{0.3}Zr_{0.7}O_2$	91
9 wt.% $V_2O_5/Ce_{0.3}Zr_{0.7}O_2$	67
6 wt.% $V_2O_5/Ce_{0.3}Zr_{0.7}O_2$ (used)	83

[a] The $Ce_{0.3}Zr_{0.7}O_2$ was prepared with hydrothermal method.

2.3. Catalytic test

The catalytic dehydrogenation of ethylbenzene in the presence of CO_2 was carried out in a fixed-bed reactor (6 mm, i.d.) under atmospheric pressure. Typically, 0.5 g of catalyst (40–60 mesh) diluted with the same amount of quartz sands was loaded into the reactor. Priori to reaction, the catalyst was pretreated at the reaction temperature for 0.5 h under a flow of CO_2. The analytical grade ethylbenzene was introduced into the reactor with an HPLC pump. The reaction parameters of W/F and CO_2/EB molar ratio were kept at constant of 7.25 g h mol^{-1} and 20, respectively. The condensed products including benzene, toluene, styrene, and unreacted ethylbenzene were analyzed on a gas chromatograph (Shimadzu GC-14B) equipped with a DB-1 capillary column (0.25 mm × 60 m) and an FID detector. The ethylbenzene conversion and styrene selectivity were calculated based on the calibrated GC peak areas of the components in liquid phase. The relative deactivation rate of the catalysts at the initial three hours was calculated using the equation of $R3 = 100 \times (X_1 - X_3)/X_1$, where X_1 and X_3 are the ethylbenzene conversion at time on stream (TOS) of 1 and 3 h, respectively.

3. Results

3.1. Surface area

The BET specific surface areas of the selected samples are given in Tables 1 and 2. Irrespective of the Ce/Zr ratios, the $Ce_xZr_{(1-x)}O_2$ prepared with hydrothermal method ($Ce_xZr_{(1-x)}O_2$–H) produced a much higher surface area than that prepared with the sol–gel method ($Ce_xZr_{(1-x)}O_2$–S). Nevertheless, the relationship between the surface area and the Ce/Zr ratio was independent of the preparation method of the solid solution. Irrespective of the preparation methods, the maximum surface area was observed for the samples with a Ce/Zr ratio of 1. After loading 3 wt.% V_2O_5 on the $Ce_{0.3}Zr_{0.7}O_2$–H, as shown in Table 2, a clear decrease of the surface area was observed due to the pore filling effect. In contrast, with the further increase of the vanadia loadings, the surface area was not decreased linearly, suggesting that vanadium species may be present with different forms. It is noteworthy that the surface areas of the catalysts such as 6 wt.% $V_2O_5/Ce_{0.3}Zr_{0.7}O_2$ were basically not changed after reaction for 6 h.

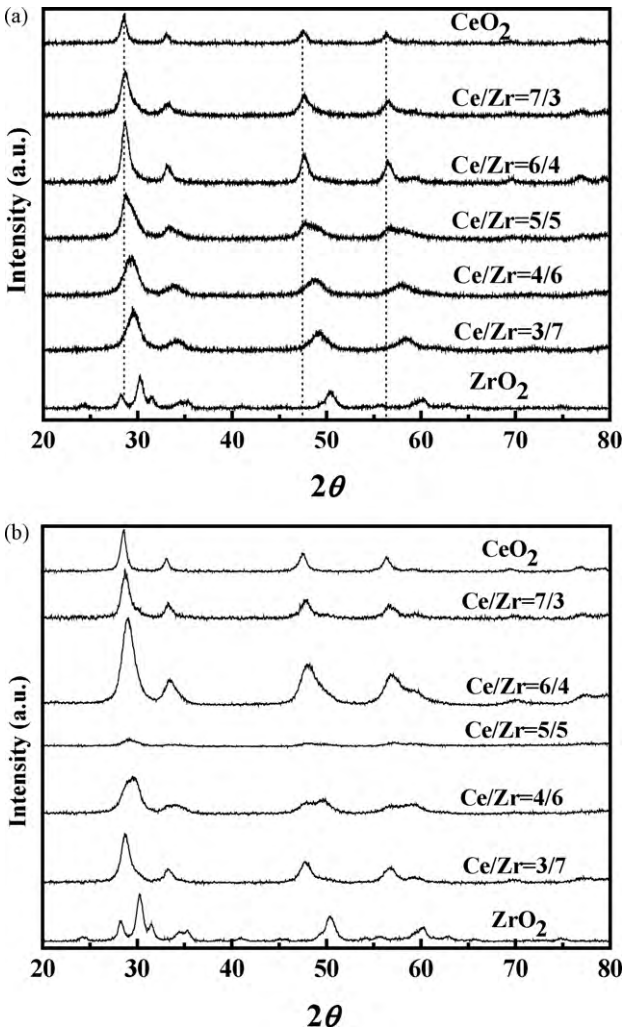

Fig. 1. XRD patterns of the $Ce_xZr_{(1-x)}O_2$ prepared with (a) hydrothermal method and (b) sol–gel method.

3.2. Crystal structure

The XRD patterns of the $Ce_xZr_{(1-x)}O_2$ are given in Fig. 1. For a comparative purpose, the CeO_2 and the ZrO_2 are also included in Fig. 1. Irrespective of the compositions and preparation methods of the $Ce_xZr_{(1-x)}O_2$, the diffraction lines in the XRD patterns assigned either to pure CeO_2 or ZrO_2 were not observed, indicating that solid solutions of $Ce_xZr_{(1-x)}O_2$ were exclusively formed as shown in Fig. 1. Moreover, in comparison with the characteristic diffractions of the cubic CeO_2 at 2θ of about 28.6, 47.5, and 56.3°, the corresponding peaks for the solid solutions were progressively shifted to higher values with decreasing the Ce/Zr molar ratios in the solid solution. The ionic diameter of Ce^{4+} is slightly larger than that of Zr^{4+}. Consequently, the lattice parameter of the solid solution was decreased with the insertion of more Zr^{4+} into the CeO_2 lattice, i.e., a lower Ce/Zr molar ratio, leading to the observed phenomena. The crystal sizes of all the solid solutions calculated by using Scherrer formula based on the diffractions at 2θ of about 29 and 48° were less than 10 nm despite the fact that it was slightly dependent on the composition and preparation methods, indicative of a nanocrystalline nature of the solid solutions. As shown in Fig. 1a, it is interesting that the intensity of the XRD diffractions of the $Ce_{0.5}Zr_{0.5}O_2$–S was extremely low in comparison with other compositions.

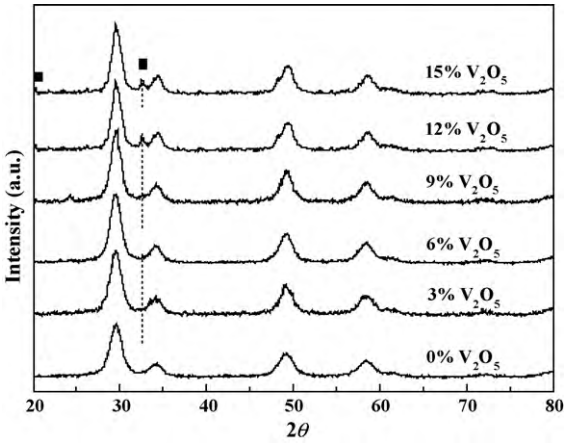

Fig. 2. XRD patterns of the $V_2O_5/Ce_{0.3}Zr_{0.7}O_2$–H as a function of the V_2O_5 loading (■: $CeVO_4$).

After loading different amounts of vanadia, no observable changes occurred for the structure of the $Ce_xZr_{(1-x)}O_2$. This is illustrated from the XRD patterns of the $V_2O_5/Ce_{0.3}Zr_{0.7}O_2$–H as shown in Fig. 2. It is clear that no crystalline V_2O_5 was detected for all the samples. Moreover, any XRD diffractions assigned to vanadium species were not observed when the vanadia loading was lower than 12 wt.%, indicating that vanadium species are well dispersed over the $Ce_{0.3}Zr_{0.7}O_2$–H. Nevertheless, new XRD peaks at 2θ of about 20.3 and 32.5° assigned to the $CeVO_4$ phase appeared when the V_2O_5 loading was greater than or equal to 12 wt.%. This implies that solid reactions occurred between the loaded vanadium species and the cerium in the $Ce_{0.3}Zr_{0.7}O_2$–H.

As it is difficult to determine the exact phase structure of the $Ce_xZr_{(1-x)}O_2$ and the state of the vanadium species based only on XRD results, Raman characterization with much higher sensitivity to vanadium species was carried out, and the results are given in Figs. 3–5, respectively. From Fig. 3, only a sharp peak at about 465 cm^{-1}, which is the characteristic Raman shift of the fluorite structure (*Fm3m* space group), was observed for the $Ce_xZr_{(1-x)}O_2$–H. Moreover, the peak intensity was clearly decreased when the Ce/Zr molar ratios were decreased from 7/3 to 3/7. This can be well explained as that the deformation of the cubic CeO_2 is increased with the insertion of more Zr^{4+}, which is reported to affect the redox properties of the mixed oxides [18]. This indicates that solid solution with pure cubic structure was formed for the $Ce_xZr_{(1-x)}O_2$–H regardless of the Ce/Zr molar ratios. In contrast, in the case of the $Ce_xZr_{(1-x)}O_2$–S, additional weak peaks at about 141, 260, 313, and 630 cm^{-1} were also observed besides the intense peak

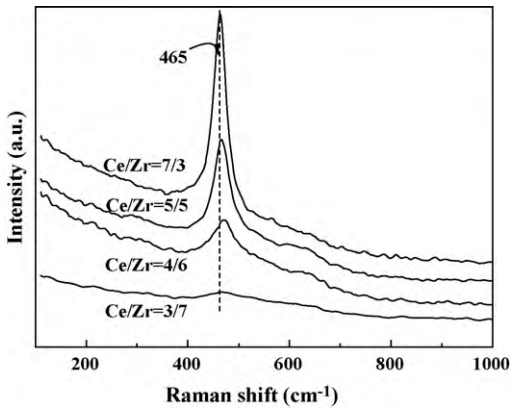

Fig. 3. Raman spectra of the $Ce_xZr_{(1-x)}O_2$ prepared with hydrothermal method.

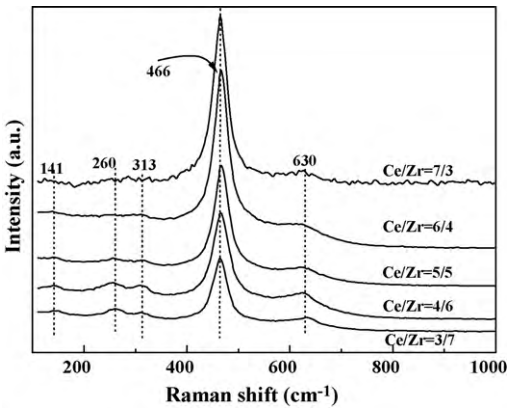

Fig. 4. Raman spectra of the $Ce_xZr_{(1-x)}O_2$ prepared with sol–gel method.

at about 466 cm^{-1} in the Raman spectra (Fig. 4). These weak peaks were attributed to either tetragonal phase (*P4₂/nmc* space group) [19] or pseudo-cubic t" phase [20]. Based on the XRD and Raman results, it is conclusive that solid solutions of the $Ce_xZr_{(1-x)}O_2$ without the separated CeO_2 or ZrO_2 are formed although the crystal structure of the solid solution is affected by the preparation methods.

The Raman spectra of the $V_2O_5/Ce_xZr_{(1-x)}O_2$ catalysts are shown in Fig. 5. The Raman shifts of the $Ce_xZr_{(1-x)}O_2$ decreased significantly after loading of V_2O_5. Based on this and the very fewer Raman shifts of the $Ce_xZr_{(1-x)}O_2$, the assignments of the Raman shifts to vanadium species become simplified. For the $V_2O_5/Ce_{0.7}Zr_{0.3}O_2$–S (Fig. 5a), different forms of vanadium species were found from the Raman spectra. The Raman bands at 793 and 857 cm^{-1} were

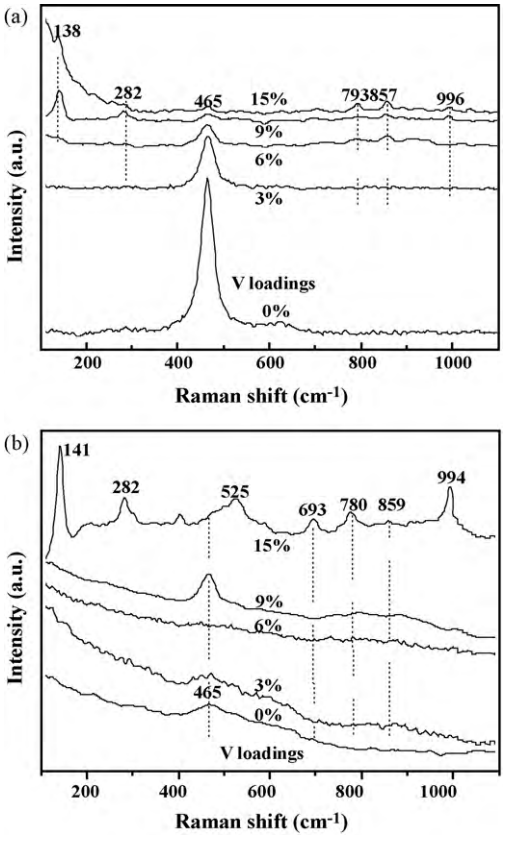

Fig. 5. Raman spectra of the $V_2O_5/Ce_{0.7}Zr_{0.3}O_2$–S (a) and the $V_2O_5/Ce_{0.3}Zr_{0.7}O_2$–H (b) as a function of the V_2O_5 loading.

Table 3
The VO_x surface densities of the $V_2O_5/Ce_xZr_{(1-x)}O_2$ catalysts.

Catalysts		VO_x surface density (atoms/nm^2)[a]
Sol-geled $Ce_{0.7}Zr_{0.3}O_2$	3 wt.% V_2O_5	2.64
	6 wt.% V_2O_5	5.29
	9 wt.% V_2O_5	7.93
	15 wt.% V_2O_5	13.22
Hydrothermal $Ce_{0.3}Zr_{0.7}O_2$	3 wt.% V_2O_5	1.56
	6 wt.% V_2O_5	3.11
	9 wt.% V_2O_5	4.67
	15 wt.% V_2O_5	7.78

[a] Calculated based on the surface area of the $Ce_xZr_{(1-x)}O_2$.

assigned to the stretching modes of V–O–V in polymeric VO_x species, and the 138, 282, and 996 cm^{-1} Raman shifts were due to the stretching vibration of the V=O bond in the bulk crystalline V_2O_5. Thus, crystalline V_2O_5, monomeric and/or polymeric VO_x species were formed over the $V_2O_5/Ce_{0.7}Zr_{0.3}O_2$–S when the V_2O_5 loadings were 9 wt.% and above. In contrast, only monomeric and/or polymeric VO_x species were present when the V_2O_5 loadings were lower than or equal to 6 wt.%. For the supported vanadia, it is well established that the polymerization degree of the surface VO_x species increases with the increasing of the VO_x surface densities, and the crystalline V_2O_5 is significant only above the monolayer surface coverage [15,21]. Moreover, the VO_x surface densities of the theoretical monolayer for the monovanadate and the polyvanadate are calculated to be 2.3 and 7.5 VO_x/nm^2, respectively [22]. Thus, the VO_x surface densities of the $V_2O_5/Ce_xZr_{(1-x)}O_2$ were calculated, and the results are given in Table 3. It is clear that the VO_x surface densities of the 9 and 15 wt.% $V_2O_5/Ce_{0.7}Zr_{0.3}O_2$–S were obviously higher than that of the theoretical monolayer for the polyvanadate. Thus, crystalline V_2O_5 was formed and detected by Raman. In the cases of the $V_2O_5/Ce_{0.3}Zr_{0.7}O_2$–H, no significant Raman shifts due to vanadium species were observed when the V_2O_5 loadings were below 9 wt.% (Fig. 5b). This is mainly due to the strong fluorescence and the much lower VO_x surface densities of the catalysts (Table 3) originated from the much higher surface areas of the $Ce_{0.3}Zr_{0.7}O_2$–H (Table 1). The Raman shift at 465 cm^{-1} for the 9 wt.% $V_2O_5/Ce_{0.3}Zr_{0.7}O_2$–H was very possibly due to the asymmetric bending mode of the isolated surface VO_x, which is supported by the fact that the Raman shifts of the $Ce_xZr_{(1-x)}O_2$ decrease significantly after loading of V_2O_5. Moreover, this is also agreeable with the reference result [21]. In contrast, for the 15 wt.% $V_2O_5/Ce_{0.3}Zr_{0.7}O_2$–H, crystalline V_2O_5 (Raman shifts at 141, 282, and 994 cm^{-1}) together with the monomeric and/or polymeric surface VO_x species (shifts at 525, 693, 780, and 859 cm^{-1}) were clearly observed, which is agreeable with the results of the VO_x surface density (Table 3). Thus, combining the XRD and Raman results, the crystal structure of the oxides and the forms of the vanadium species over the $V_2O_5/Ce_xZr_{(1-x)}O_2$ can be determined.

3.3. Reduction behavior

The chemical properties of the multi-metal oxides can be convincingly probed by TPR, which reveals not only the reducibility but also the surface chemical interactions between different oxides. For the bulk V_2O_5, three well-separated TPR peaks at 965, 1003 and 1067 K corresponding to the sequential reduction of V_2O_5 to V_6O_{13}, V_6O_{13} to V_2O_4 and V_2O_4 to V_2O_3, respectively, were observed [23,24]. In contrast, the TPR patterns of the oxide-supported V_2O_5 always show a single peak at much lower reduction temperatures, in which the temperature at peak maximum is strongly dependent on the oxide support used [24–26]. This holds true for the $V_2O_5/Ce_xZr_{(1-x)}O_2$ catalysts irrespective of the preparation methods and the Ce/Zr ratios. The effect of V_2O_5 loadings on

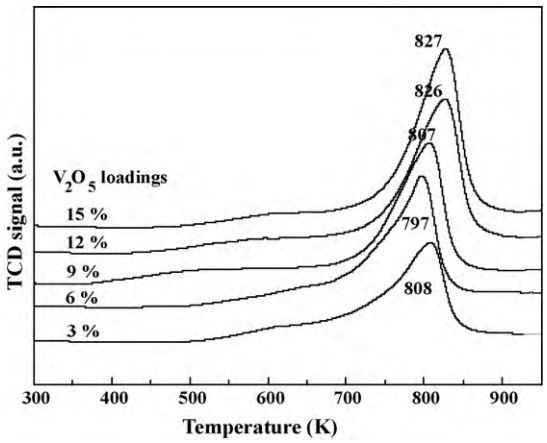

Fig. 6. The temperature-programmed reduction behavior of the hydrothermally synthesized $Ce_{0.3}Zr_{0.7}O_2$ with different V_2O_5 loadings.

the reduction behavior of the $V_2O_5/Ce_{0.3}Zr_{0.7}O_2$–H is illustrated in Fig. 6. It is clear that the intensity and area of the TPR peaks increased with the increase of the V_2O_5 loadings. However, there was no linear relationship between the peak intensity and the V_2O_5 loadings. Moreover, the reduction temperature at the peak maximum shifted as a function of the V_2O_5 loadings, i.e., to lower temperatures and then back to higher temperatures, which are agreeable with the reported results over the V_2O_5/Al_2O_3 [26]. Generally, the supported vanadium species with larger size and random orientation show higher reduction temperature. Furthermore, the crystallized V_2O_5 gives a higher reduction temperature than the monomeric or polymeric vanadates. Thus, in combination with the Raman spectroscopic results, the present TPR results are well understandable.

3.4. Catalytic results

To determine the optimal calcination temperature of the catalyst, the 6 wt.% $V_2O_5/Ce_{0.4}Zr_{0.6}O_2$–S was selected and calcined at various temperatures. The catalytic results are given in Fig. 7. Under the conditions investigated, very high ST selectivity of greater than 95% was achieved. However, different features were found in the case of the EB conversion. Increasing the calcination temperature of the catalyst from 773 to 823 K, there was basically no influence on the EB conversion under the reaction conditions investigated. On the contrary, nontrivial decrease of the EB conversion was found when the calcination temperature was further increased. In comparison with the EB conversions at lower reaction temperatures of 823 or 873 K, the clearly decreased EB conversion at 923 K was due to the faster deactivation of the catalyst at higher reaction temperature. Thus, the optimal calcination temperature of the catalyst was determined to be 823 K and applied to all the catalysts in the following.

Fig. 8 shows the catalytic results obtained over the 6 wt.% $V_2O_5/Ce_xZr_{(1-x)}O_2$. Under the conditions investigated, above 94% ST selectivity was achieved regardless of both the preparation methods and Ce/Zr molar ratios of the $Ce_xZr_{(1-x)}O_2$. At any Ce/Zr molar ratios, the 6 wt.% $V_2O_5/Ce_xZr_{(1-x)}O_2$–H gave obviously higher EB conversions than the 6 wt.% $V_2O_5/Ce_xZr_{(1-x)}O_2$–S. When the Ce/Zr molar ratio was concerned, a complex but insignificant effect was observed. In the case of the 6 wt.% $V_2O_5/Ce_xZr_{(1-x)}O_2$–H, the maximum EB conversion of about 75% was achieved over the 6 wt.% $V_2O_5/Ce_{0.4}Zr_{0.6}O_2$–H. In contrast, over the 6 wt.% $V_2O_5/Ce_xZr_{(1-x)}O_2$–S, the maximum EB conversion of about 67% was obtained over the 6 wt.% $V_2O_5/Ce_{0.3}Zr_{0.7}O_2$–S. Thus, the activity of the 6 wt.% $V_2O_5/Ce_xZr_{(1-x)}O_2$ was strongly dependent on both

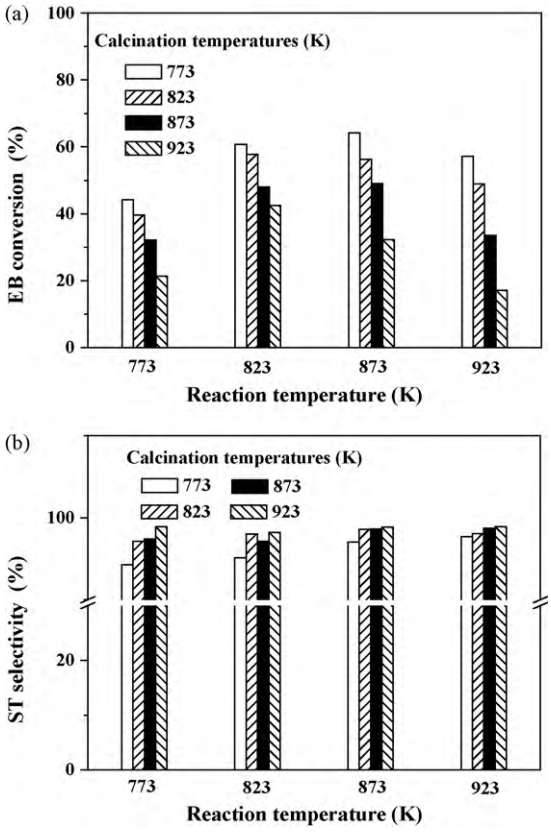

Fig. 7. The effect of calcination temperature of the 6 wt.% $V_2O_5/Ce_{0.4}Zr_{0.6}O_2$–S on its catalytic performance indexed by (a) EB conversion and (b) ST selectivity under the reaction conditions of P = 1 atm, W/F = 7.25 g h mol^{-1}, CO_2/EB (molar ratio) = 20/1, and TOS = 1 h.

the Ce/Zr molar ratios and the preparation methods of the solid solution.

Fig. 9 shows the TOS results of the titled reaction over the 6 wt.% $V_2O_5/Ce_xZr_{(1-x)}O_2$ catalysts. It is clear that a stable ST selectivity of 98% was observed for all the catalysts. However, the EB conversion was decreased at different degrees depending on the catalyst used. Generally, the 6 wt.% $V_2O_5/Ce_xZr_{(1-x)}O_2$–H was more stable than the 6 wt.% $V_2O_5/Ce_xZr_{(1-x)}O_2$–S as indexed by the EB conversion. Moreover, this can be clearly reflected from the data of the relatively deactivation rate shown in Table 4. Significantly, the 6 wt.% $V_2O_5/Ce_{0.3}Zr_{0.7}O_2$–H showed the lowest R3, indicating its best stability among the catalysts investigated. Thus, the $Ce_{0.3}Zr_{0.7}O_2$–H was used to study the effect of V_2O_5 loadings on the catalytic performance, and the results are illustrated in Fig. 10. For comparison, the catalytic results over the $Ce_{0.3}Zr_{0.7}O_2$–H are also included. Clearly, the TOS stability of the EB conversion increased with increasing V_2O_5 loadings from 3 to 6 wt.%, but decreased when the V_2O_5

Table 4
Summary of the relative deactivation rates of various catalysts.

Catalysts	R3 (%)[a]
6 wt.% $V_2O_5/Ce_{0.3}Zr_{0.7}O_2$–S	54.7
6 wt.% $V_2O_5/Ce_{0.4}Zr_{0.6}O_2$–S	46.7
6 wt.% $V_2O_5/Ce_{0.7}Zr_{0.3}O_2$–S	48.0
6 wt.% $V_2O_5/Ce_{0.3}Zr_{0.7}O_2$–H	24.8
6 wt.% $V_2O_5/Ce_{0.4}Zr_{0.6}O_2$–H	33.9
6 wt.% $V_2O_5/Ce_{0.5}Zr_{0.5}O_2$–H	31.9
6 wt.% $V_2O_5/Ce_{0.6}Zr_{0.4}O_2$–H	52.7
6 wt.% $V_2O_5/Ce_{0.7}Zr_{0.3}O_2$–H	55.1

[a] R3 = 100 × ($X_1 - X_3$)/X_1, where X_1 and X_3 are EB conversions at TOS of 1 and 3 h, respectively.

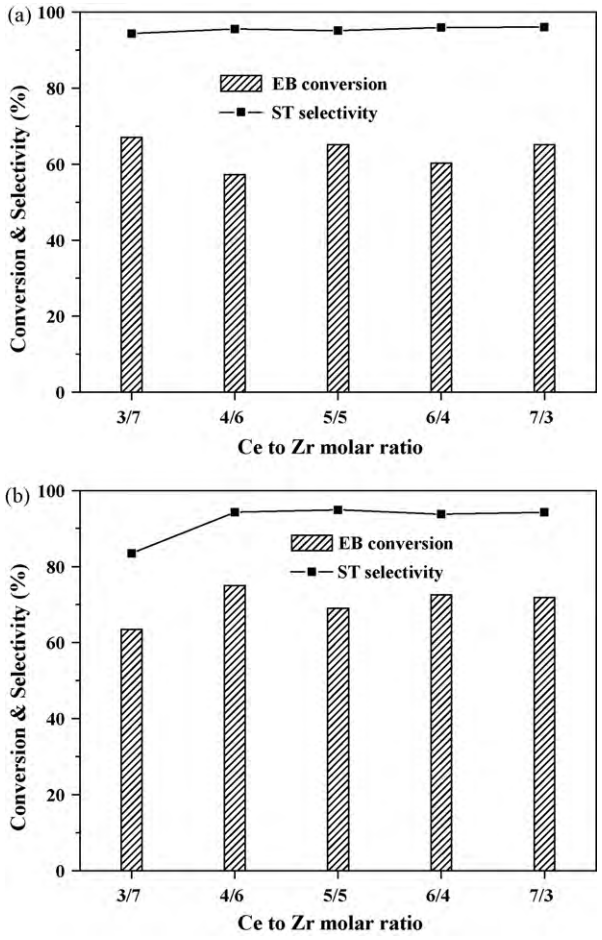

Fig. 8. The effect of Ce/Zr molar ratios on the EB conversion and ST selectivity over the 6 wt.% $V_2O_5/Ce_xZr_{(1-x)}O_2$ prepared with (a) sol–gel method and (b) hydrothermal method. (The reaction conditions: T = 823 K, P = 1 atm, W/F = 7.25 g h mol^{-1}, CO_2/EB (molar ratio) = 20/1, TOS = 1 h).

loadings was further increased until 15 wt.%. Moreover, a stable ST selectivity of about 98% was obtained after TOS of 2 h for all the V_2O_5 loaded catalysts. Although the $Ce_{0.3}Zr_{0.7}O_2$–H showed a TOS EB conversion similar to that of the 6 wt.%$V_2O_5/Ce_{0.3}Zr_{0.7}O_2$–H, the ST selectivity reached about 98% after TOS of 6 h. Considering

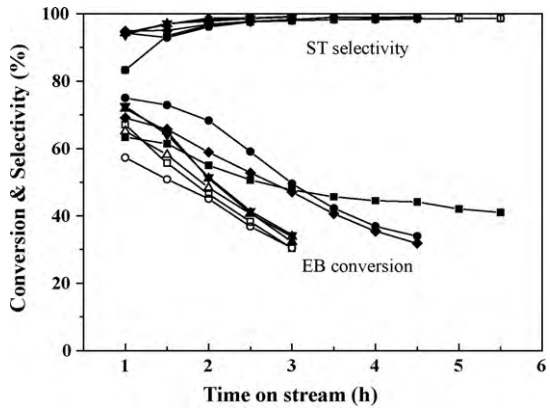

Fig. 9. The time-on-stream catalytic behavior over the 6 wt.% $V_2O_5/Ce_xZr_{(1-x)}O_2$ under the reaction conditions of T = 823 K, P = 1 atm, W/F = 7.25 g h mol^{-1}, CO_2/EB (molar ratio) = 20/1 (open symbols for the $Ce_xZr_{(1-x)}O_2$–S; filled symbols for the $Ce_xZr_{(1-x)}O_2$–H. ▲△, Ce/Zr = 7/3; ▼, Ce/Zr = 6/4; ♦, Ce/Zr = 5/5; ●○, Ce/Zr = 4/6; ■□, Ce/Zr = 3/7).

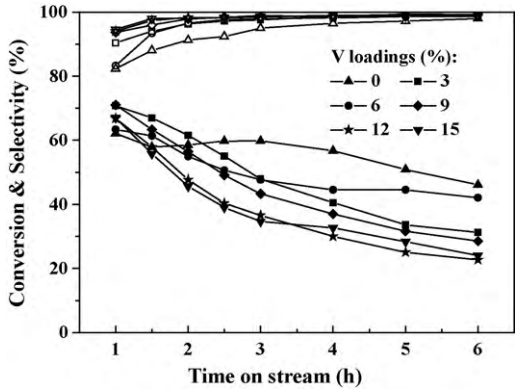

Fig. 10. The effect of V_2O_5 loadings on the TOS performance of the $V_2O_5/Ce_{0.3}Zr_{0.7}O_2$–H towards the titled reaction under the conditions of T = 823 K, P = 1 atm, W/F = 7.25 g h mol^{-1}, CO_2/EB (molar ratio) = 20/1 (open symbols: ST selectivity; filled symbols: EB conversion).

both the EB conversion and ST selectivity, 6 wt.%$V_2O_5/Ce_{0.3}Zr_{0.7}O_2$ should be the choice for the titled reaction.

4. Discussion

Due to the platelet morphology and inactive basal planes, crystalline V_2O_5 shows very low activity for the oxidative dehydrogenation reactions [15]. For the oxide-supported V_2O_5, it is generally observed that crystalline V_2O_5 becomes significant only above the monolayer surface coverage, which is agreeable with our results over the $V_2O_5/Ce_xZr_{1-x}O_2$ (Fig. 5 and Table 3). Thus, highly dispersed surface VO_x species without the formation of crystalline V_2O_5 are responsible for the high activity of the $V_2O_5/Ce_xZr_{1-x}O_2$. The results shown in Figs. 8 and 9 are agreeable with the claim. In the case of the 3 wt.% $V_2O_5/Ce_{0.3}Zr_{0.7}O_2$–H, the surface VO_x density (1.56 VO_x/nm^2) was much lower than the theoretical monolayer coverage of the monovanadate (2.3 VO_x/nm^2), and highly dispersed VO_x was confirmed from Raman results (Fig. 5b), leading to its high activity towards the titled reaction. In contrast, clearly lower EB conversion over the 15 wt.% $V_2O_5/Ce_{0.3}Zr_{0.7}O_2$–H at the initial reaction stage than those over the 3 wt.% $V_2O_5/Ce_{0.3}Zr_{0.7}O_2$–H was found (Fig. 10) although the amount of vanadia over the 15 wt.% $V_2O_5/Ce_{0.3}Zr_{0.7}O_2$–H was much higher, which is due to the formation of crystalline V_2O_5 and the lowered dispersion of the surface VO_x species over the 15 wt.% $V_2O_5/Ce_{0.3}Zr_{0.7}O_2$–H. Moreover, as a result of the much higher surface areas of the $Ce_xZr_{1-x}O_2$–H than the $Ce_xZr_{1-x}O_2$–S (Table 1), the VO_x surface densities of the 6 wt.% $V_2O_5/Ce_xZr_{1-x}O_2$–H were much lower than those of the 6 wt.% $V_2O_5/Ce_xZr_{1-x}O_2$–S (Table 3), leading to the generally higher EB conversion over the 6 wt.% $V_2O_5/Ce_xZr_{1-x}O_2$–H (Fig. 8). Thus, the clear effect of the $Ce_xZr_{1-x}O_2$ on the activity of the titled reaction over the $V_2O_5/Ce_xZr_{1-x}O_2$ is mainly due to the dispersion of the VO_x species over the $Ce_xZr_{1-x}O_2$.

It is a common fact that the redox properties of the $Ce_xZr_{1-x}O_2$ are closely related to the Ce/Zr ratios and crystal structure determined by the preparation methods. Recently, it is revealed that the surface and bulk concentration of the Ce^{4+}–O–Ce^{3+}-type defects of the nano ceria is strongly dependent on the preparation methods of the oxide, and the activation of EB by surface Ce^{4+}–O–Ce^{3+} defects is responsible for the oxidative dehydrogenation of EB with N_2O [17]. Raman spectra (Figs. 3 and 4) clearly indicate the differences in the crystal structure of the solid solutions prepared with different methods, i.e., pure cubic structure for the $Ce_xZr_{1-x}O_2$–H and mixed phases for the $Ce_xZr_{1-x}O_2$–S. Moreover, the intensity of the Raman shift at about 465 cm^{-1}, which affects the redox properties of the solid solution, is significantly varied with both the Ce/Zr ratios and

Table 5
Summary of the TGA/DSC results for the used catalysts[a].

	Temperature (K)[b]	Weight loss (%)
$Ce_{0.3}Zr_{0.7}O_2$	550	7.6
3 wt.% $V_2O_5/Ce_{0.3}Zr_{0.7}O_2$	581	7.2
6 wt.% $V_2O_5/Ce_{0.3}Zr_{0.7}O_2$	593	7.1
15 wt.% $V_2O_5/Ce_{0.3}Zr_{0.7}O_2$	624	4.1

[a] The $Ce_{0.3}Zr_{0.7}O_2$ was prepared with hydrothermal method, and the catalysts were tested for 6 h under the conditions of CO_2/EB = 20, W/F = 7.25 g-cat h mol^{-1}, and T = 823 K.
[b] The peak temperature at maximum heat flow.

the preparation methods of the solid solutions (Figs. 3 and 4). Thus, based on these facts and the redox mechanism of the titled reaction [14], the effect of Ce/Zr ratio on the EB conversion over the $V_2O_5/Ce_xZr_{1-x}O_2$ (Fig. 8) may also be contributed from the differences in the phase structure of the solid solutions.

Although all the catalysts showed relatively fast deactivation, the deactivation rate is clearly dependent on the vanadia loadings. As shown in Table 2, the BET surface area of the used catalyst was quite similar to that of the fresh catalyst, indicating that the loss of BET surface plays a less important role for the catalyst deactivation if it has. To find out the reasons, TGA/DSC was applied to analyze the carbon deposition over the used catalysts, and the results are summarized in Table 5. The amount of carbonaceous materials deposited over the catalyst was decreased with increasing the vanadia loadings, especially in the case of the 15 wt.% $V_2O_5/Ce_{0.3}Zr_{0.7}O_2$. In contrast, the peak temperature for burning the deposited carbon was continuously increased with increasing the V_2O_5 loadings, indicating an increase in the C/H ratios of the deposited carbon. Thus, carbon deposition was inhibited while the C/H ratio in the deposited carbon was increased with the increase of the V_2O_5 loadings. Based on these facts, it can be deduced that the aging of the deposited carbon (increasing in C/H ratios) may be the main factor for the deactivation of the $V_2O_5/Ce_xZr_{1-x}O_2$.

It should be noted that the relative fast deactivation of the catalyst is really unexpected to us. This forced us to think that the interface properties of VO_x and $Ce_xZr_{1-x}O_2$ may play a role in determining its catalytic activity and stability for the titled reaction. Indeed, in a recent work, the stabilization of the small V^{5+} species at sub-monolayer surface coverage by ceria is convincingly proved to be a crucial factor for its enhanced activity towards the oxidative dehydrogenation reactions [27]. Thus, it may be expected that a catalyst with well-controlled VO_x species interfaced with $Ce_xZr_{1-x}O_2$ via wetting a high surface area oxide such as mesoporous alumina shows improved performance for the titled reaction, and is worthy to be investigated.

5. Conclusions

Based on the above results and discussion, the conclusions drawn from this work are summarized as follows:

(1) Independent on the Ce/Zr molar ratios and the preparation methods, the solid solution of $Ce_xZr_{1-x}O_2$ was exclusively formed. At the same time, the BET surface areas of the $Ce_xZr_{1-x}O_2$–H (~110–130 m^2/g) were significantly higher than those of the $Ce_xZr_{1-x}O_2$–S (~65–95 m^2/g). The $Ce_xZr_{1-x}O_2$–H showed pure cubic structure while the $Ce_xZr_{1-x}O_2$–S samples had mixed phases. In the case of the $V_2O_5/Ce_xZr_{1-x}O_2$ catalysts, highly dispersed VO_x species were detected at low vanadia loadings while surface VO_x species and crystalline V_2O_5 were formed at higher V_2O_5 loadings. Nevertheless, all the V_2O_5-based catalysts showed one-step reduction of the vanadia at the reaction temperature of the titled reaction although the reduction temperatures at peak maximum strongly depended on the V_2O_5 loadings.
(2) A clear and complex promotional effect of the $Ce_xZr_{1-x}O_2$ on V_2O_5 for catalyzing the titled reaction was observed. Generally, the $V_2O_5/Ce_xZr_{1-x}O_2$–H showed obviously higher initial EB conversion than the $V_2O_5/Ce_xZr_{1-x}O_2$–S although quite similar ST selectivity was obtained. In terms of both the TOS EB conversion and ST selectivity, the 6 wt.% $V_2O_5/Ce_{0.3}Zr_{0.7}O_2$–H showed better catalytic performance.
(3) Depending on the Ce/Zr ratios, preparation methods, and vanadia loadings, the activity and stability of the $V_2O_5/Ce_xZr_{1-x}O_2$ were discussed based on the experimental and characterization results. The dispersion of the surface VO_x species and aging of the deposited coke on the catalysts were revealed to be the main factors responsible for the activity and stability of the $V_2O_5/Ce_xZr_{1-x}O_2$, and a suggestion for developing a high-performance $V_2O_5/Ce_xZr_{1-x}O_2$ catalyst was proposed.

Acknowledgement

The financial support by the Program for New Century Excellent Talents in University (NCET-08-0799) is highly acknowledged.

References

[1] K. Saito, K. Okuda, N. Ikenaga, T. Miyake, T. Suzuki, J. Phys. Chem. A 114 (2010) 3845.
[2] X. Ye, Y. Yue, C. Miao, Z. Xie, W. Hua, Z. Gao, Green Chem. 7 (2005) 524.
[3] B.M. Reddy, H. Jin, D.-S. Han, S.-E. Park, Catal. Lett. 124 (2008) 357.
[4] S. Chen, Z. Qin, A. Sun, J. Wang, J. Nat. Gas Chem. 15 (2006) 11.
[5] D.R. Burri, K.-M. Choi, D.-S. Han, Sujandi, N. Jiang, A. Burri, S.-E. Park, Catal. Today 131 (2008) 173.
[6] B.M. Reddy, D.-S. Han, N. Jiang, S.-E. Park, Catal. Surv. Asia 12 (2008) 56.
[7] Y. Sakurai, T. Suzaki, N. Ikenaga, T. Suzuki, Appl. Catal. A: Gen. 192 (2000) 281.
[8] A. Sun, Z. Qin, S. Chen, J. Wang, Catal. Today 93–95 (2004) 273.
[9] T. Badstube, H. Pappa, R. Dziembaj, P. Kustrowski, Appl. Catal. A: Gen. 204 (2000) 153.
[10] V.P. Vislovskiy, J.-S. Chang, M.-S. Park, S.-E. Park, Catal. Commun. 3 (2002) 227.
[11] D.-Y. Hong, V.P. Vislovskiy, Y. Hwang, S. Jhung, J.-S. Chang, Catal. Today 131 (2008) 140.
[12] B. Xiang, C. Yu, H. Xu, W. Li, Catal. Lett. 125 (2008) 90.
[13] S. Chen, Z. Qin, X. Xu, J. Wang, Appl. Catal. A: Gen. 302 (2006) 185.
[14] M.-S. Park, V.P. Vislovskiy, J.-S. Chang, Y.-G. Shul, J.S. Yoo, S.-E. Park, Catal. Today 87 (2003) 205.
[15] I.E. Wachs, Catal. Today 100 (2005) 79.
[16] J. Kaspar, P. Fornasiero, M. Graziani, Catal. Today 50 (1999) 285.
[17] B. Murugan, A.V. Ramaswamy, J. Am. Chem. Soc. 129 (2007) 3062.
[18] I. Atribak, A. Bueno-Lopez, A. Garcia-Garcia, J. Catal. 259 (2008) 123.
[19] X. Wu, X. Wu, Q. Liang, J. Fan, D. Weng, Z. Xie, S. Wei, Solid State Sci. 9 (2007) 636.
[20] M. Fernandez-Garcia, A. Martinez-Arias, A. Iglesias-Juez, C. Belver, A.B. Hungria, J.C. Conesa, J. Soria, J. Catal. 194 (2000) 385.
[21] H. Tian, E.I. Ross, I.E. Wachs, J. Phys. Chem. B 110 (2006) 9593.
[22] A. Khodakov, B. Olthof, A.T. Bell, E. Iglesia, J. Catal. 181 (1999) 205.
[23] M.M. Koranne, J.G. Goodwin Jr., G. Marcelin, J. Catal. 148 (1994) 369.
[24] K.V.R. Chary, C.P. Kumar, D. Naresh, T. Bhaskar, Y. Sakata, J. Mol. Catal. A: Chem. 243 (2006) 149.
[25] Y. Sakurai, T. Suzaki, K. Nakagawa, N. Ikenaga, H. Aota, T. Suzuki, J. Catal. 209 (2002) 16.
[26] Z. Wu, H.-S. Kim, P.C. Stair, S. Rugmini, S.D. Jackson, J. Phys. Chem. B 109 (2005) 2793.
[27] M. Baron, H. Abbott, O. Bondarchuk, D. Stacchiola, A. Uhl, S. Shaikhutdinov, H.-J. Freund, C. Popa, M.V. Ganduglia- Pirovano, J. Sauer, Angew. Chem. Int. Ed. 48 (2009) 8006.